**PAPER**

View Article Online
View Journal | View Issue

# Effect of the alkali insertion ion on the electrochemical properties of nickel hexacyanoferrate electrodes

Hyun-Wook Lee,[a] Mauro Pasta,[a] Richard Y. Wang,[a] Riccardo Ruffo[b] and Yi Cui*[ac]

Nickel hexacyanoferrate (NiHCFe) is an attractive cathode material in both aqueous and organic electrolytes due to a low-cost synthesis using earth-abundant precursors and also due to its open framework, Prussian blue-like crystal structure that enables ultra-long cycle life, high energy efficiency, and high power capability. Herein, we explored the effect of different alkali ions on the insertion electrochemistry of NiHCFe in aqueous and propylene carbonate-based electrolytes. The large channel diameter of the structure offers fast solid-state diffusion of $Li^+$, $Na^+$, and $K^+$ ions in aqueous electrolytes. However, all alkali ions in organic electrolytes and $Rb^+$ and $Cs^+$ in aqueous electrolytes show a quasi-reversible electrochemical behavior that results in poor galvanostatic cycling performance. Kinetic regimes in aqueous electrolyte were also determined, highlighting the effect of the size of the alkali ion on the electrochemical properties.

## Introduction

The demand for advanced energy storage devices has greatly increased recently, and current research efforts focus on solving scientific issues associated with this formidable challenge.[1,2] Depending on the targeted application, researchers in this area look for improvements in power output[3,4] and energy density[5,6] for portable applications and for cycle/calendar life and cost for grid-scale stationary energy storage systems (GSES).[7–9] Li-ion batteries (LIBs) based on conventional organic electrolytes have been widely used and studied for portable applications due to their high energy density (deriving from the high operating voltage and low electrochemical equivalent weight of lithium) and reasonable durability, which allow them to meet current market requirements.[10] Nevertheless, the constant

[a]*Department of Materials Science and Engineering, Stanford University, Stanford, California 94305, USA. E-mail: yicui@stanford.edu*

[b]*Dipartimento di Scienza dei Materiali, Università di Milano Bicocca, via Cozzi 55 20125, Milan, Italy*

[c]*Stanford Institute for Materials and Energy Science, SLAC National Accelerator Laboratory, Menlo Park, California 94025, USA*

increase in the demand for Li raw materials and their limited availability could lead to a considerable rise in the cost of LIBs in the near future.[11] In this regard, Na or K-ion based secondary batteries are often proposed as promising alternatives due to the ready and lower-cost availability of the raw materials.[12]

In the case of GSES applications, the key performance metrics are cost, environmental compatibility, cycle life, energy efficiency, and response time rather than energy density. In fact, the $ per kW h cost of the stored energy should be comparable to the price of the energy delivered by the primary source. Therefore, long calendar life and high energy efficiencies are required to reduce their lifetime cost.[13] Aqueous rechargeable batteries can meet these requirements, and previous research efforts in this area have been very promising.[14–16]

Open-framework Prussian blue analogues (PBAs) have recently received a great deal of attention as alkali-ion rechargeable battery electrodes due to their impressive electrochemical cyclability, their straightforward and low-cost synthetic processes, and the possibility of using them in both aqueous and organic electrolytes.[17–19] This class of materials contains large interstitial sites that allow for the insertion of alkali[20] and divalent[21] ions with very little crystallographic lattice strain. However, the insertion of different cations results in very different electrochemical behavior in both aqueous and organic electrolytes.[22] Hence, a deeper understanding of the effect of the nature of the inserting ion in aqueous and organic electrolytes on the electrochemical features of PBAs is required to achieve improved battery performance.

Herein, we investigated the electrochemical behavior of nickel hexacyanoferrate (NiHCFe) in different aqueous and organic electrolytes with particular emphasis on the role of the guest cation. Among different PBAs, we chose NiHCFe as a model system because of its chemical stability in both water and propylene carbonate and because of its redox behavior potential well within the electrochemical stability window of the investigated electrolytes.

## Materials and methods

NiHCFe nanoparticles were prepared by a simple co-precipitation method[22,23] in which 120 mL of a 40 mM aqueous solution of $Ni(NO_3)_2$ and 120 mL of a 20 mM solution of $K_3Fe(CN)_6$ were simultaneously added dropwise into 60 mL of deionized water with vigorous stirring. The precipitation was carried out at a constant temperature of 70° C until a yellow–orange precipitate formed. The precipitate was then filtered, washed several times with deionized water, and dried under vacuum at 40° C for 12 h. High-resolution powder X-ray diffraction (XRD) patterns were obtained at 12 keV ($\lambda = 1.0332$ Å) at BL 2-1 at the Stanford Synchrotron Radiation Lightsource (SSRL) using zero-background quartz holders in reflection geometry with a monochromator and Soller slits. The structural analysis was performed on the XRD data with the Rietveld refinement method using the EXPGUI interface for the General Structure Analysis System (GSAS).[24–26] Morphology and particle size were investigated with transmission electron microscopy (TEM, Tecnai $G^2$ F20 X-Twin).

The electrochemical investigation was carried out on electrodes prepared by casting a slurry made of 80 wt% NiHCFe, 10 wt% carbon (Timcal Super P Li), and 10 wt% polyvinylidene fluoride (PVDF, Kynar HSV 900) dispersed in 1-methyl-2-pyrrolidone (NMP) on a carbon cloth (Fuel Cell Earth/Ballard AvCarb) current

collector. The electrodes were then dried under vacuum at room temperature for 10 h, resulting in an active material loading of about 8–10 mg cm$^{-2}$. The electrodes were tested in a flooded, three-electrode electrochemical cell equipped with a commercial Ag/AgCl (4 M KCl) reference electrode and an activated carbon counter electrode. In-depth kinetics experiments were carried out in a Swagelok, three-electrode cell equipped with a pseudo-reference Ag/AgCl electrode, an activated carbon counter electrode, and an active electrode – prepared by coating the surface of a stainless steel current collector with the slurry previously described, achieving an active material loading of about 1 mg cm$^{-2}$. The Ag/AgCl pseudo-reference electrode was calibrated before and after each measurement in both aqueous and organic electrolyte using a commercial Ag/AgCl 3.5 M reference electrode and the Fc$^+$/Fc$^0$ redox couple,[27] respectively. All the potentials were converted relative to the standard hydrogen electrode (SHE). 1 M aqueous solutions of LiNO$_3$, NaNO$_3$, KNO$_3$, RbNO$_3$, CsNO$_3$ and 1 M LiClO$_4$, NaClO$_4$, and 0.8 M KPF$_6$ solutions in propylene carbonate were prepared and tested. The acidity of all aqueous electrolytes was increased to a pH of 2 by the addition of HNO$_3$ to take advantage of the lower solubility of PBAs in acidic conditions.[28]

## Results and discussion

**Physicochemical characterization**

The as-synthesized NiHCFe has the general perovskite-type open framework crystal structure, shown in Fig. 1a, in which hexacyanoferrate complexes and nickel ions bound by cyanide linkages form a face-centered cubic structure. In the framework, guest cations can occupy large interstitial A sites around the center of each cube, as confirmed by high-resolution synchrotron powder diffraction measurements (Fig. 1b). Sharp peaks indicate the high crystallinity of the powder, and the absence of secondary peaks verifies the presence of a single phase and the absence of impurities. Rietveld refinement of the XRD data confirms that NiHCFe has a perovskite structure with a face-centered cubic phase ($fm\bar{3}m$, $a_0 = 10.211$ Å) that matches closely the crystal structure of Prussian blue (JCPDS no. 73-0687). The TEM image in Fig. 1c shows spherical particles with an average diameter of about 20–50 nm, which is beneficial for increasing the surface area (better contact with the electrolyte and the conductive additive) and reducing diffusion lengths of the charge carriers (both ions and electrons). In Fig. 1d and e, the HR-TEM image and its corresponding inverse fast Fourier transform (FFT) show an interplanar distance of about 2.076 Å, which well matches the (422) crystal plane.

**Effect of insertion ion and solvent on the electrochemical properties of NiHCFe**

The effect of the insertion ion on the insertion potential of NiHCFe bulk electrodes in aqueous electrolytes was investigated in a previous study by our research group.[22,23] In that study, increases in the insertion potential were observed for ions further down Group I on the periodic table. This behavior has been previously interpreted by Scholz et al.[29–31] They suggested that the change in Gibbs free energy due to the alkali ion insertion $\Delta G_i$ (corresponding to the insertion potential: $\Delta G_i = -nF\Delta E_i$) is equal to the difference between the Gibbs free energy of "solvation" of the alkali ion in the NiHCFe lattice ($\Delta G_l$) and the Gibbs free energy of solvation of the alkali ion in the solvent ($\Delta G_s$):[29]
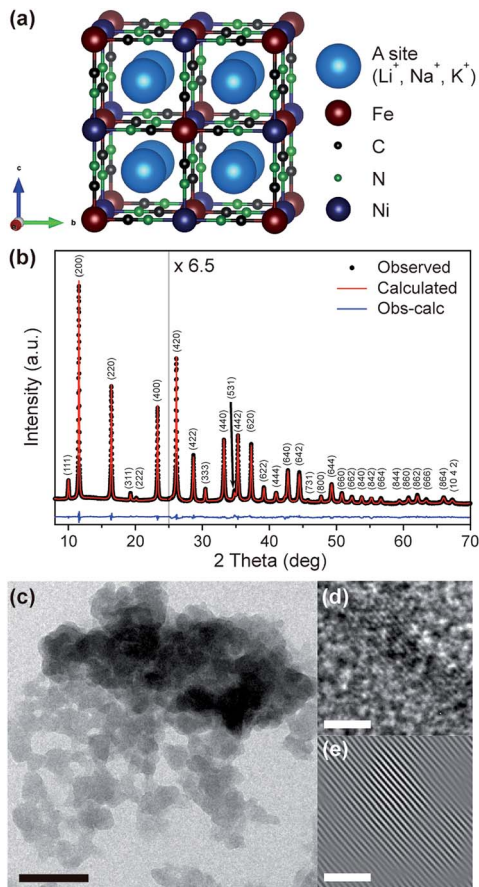
**Fig. 1** (a) Schematic illustration of the unit cell of the open-framework NiHCFe structure with carbon-coordinated Fe ions and nitrogen-coordinated Ni ions. (b) Rietveld-refined XRD data of the as-synthesized NiHCFe. Black dots and red lines indicate the observed and the calculated patterns, respectively. The blue line at the bottom indicates the difference between observed and calculated patterns. The magnified patterns (6.5×) are shown for clarity above 25°. (c) Transmission electron microscope (TEM) images (black scale bar, 100 nm) and (d) high-resolution TEM images of NiHCFe nanopowders. (e) The inverse fast Fourier transform (FFT) of (d) (white scale bar, 1 nm).

$$\Delta G_i = -nF\Delta E_i = \Delta G_l - \Delta G_s$$

$\Delta G_l$ corresponds to the free energy of any residual hydration of the alkali ion after insertion. The magnitude of this value is smaller than the free energy of solvation in solution ($\Delta G_s$) because insertion ions are mostly dehydrated as they go into the structure. Fully hydrated ions cannot fit in the interstitial sites, which are about 3.2 Å in diameter, because they are much larger in diameter.[32] Thus, the variation in insertion potential for different insertion ions is mainly a function of just the Gibbs free energy of solvation (hydration in the case of water) of the insertion ion. $\Delta G_i$ decreases as the ionic radius of the ion increases further down Group I of the

periodic table since larger ions have lower hydration energies in solution.[33] In the present study, the same behavior is observed (Fig. 2a and Table 1).

It is worth noticing the presence of multiple electrochemical processes between 0.3 and 0.8 V *versus* SHE in the case of $Li^+$ at pH 6 (Fig. 2b, blue line). Since the concentration of $H^+$ is so low in this experiment, all the peaks can be attributed to the insertion of $Li^+$. The peaks are at different potentials because of the varying levels of hydration of $Li^+$ when in the structure. This is only observed for $Li^+$ because its small ionic radius allows for a significant degree of hydration even when in the structure. In other words, $\Delta G_1$ takes on varying values for $Li^+$ and has a more significant impact on the change in Gibbs free energy for ion insertion. The reduction peak is located at the lowest potential because the ions are almost fully dehydrated as they diffuse through the channels in the framework, but once they insert into interstitial sites, they may be partially rehydrated by mobile water molecules in the structure.[29] At pH 2 (Fig. 2b, red line), we see an additional electrochemical process developing at 0.6 V that is ascribed to the insertion of hydronium ions, as confirmed by CV cycling in an acidified lithium-free cell at pH 3 (Fig. 2b, black line). Data obtained at pH 6 (Fig. 2c) clearly show the capacity fading upon cycling caused by the higher solubility of NiHCFe.[28] The solubility of NiHCFe at pH 2 and 1 M salt solution is infinitesimal and definitely not enough to affect the measurements. In the case of $K^+$ and $Na^+$ insertion, the $H_3O^+$ peak is not observed because of the higher insertion potentials of these ions,
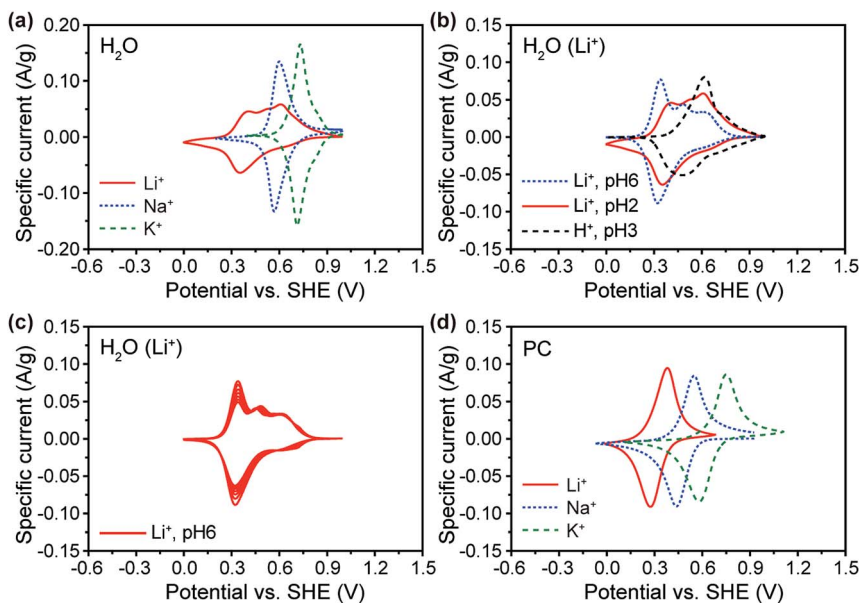


Fig. 2 Cyclic voltammetry (CV) curves of NiHCFe. The scan rate is 0.1 mV s$^{-1}$. (a) CV curves using aqueous electrolytes of $Li^+$, $Na^+$, and $K^+$ ions. (b) CV curves (in blue, red, and black) are measured by using 1 M $LiNO_3$ in $H_2O$ (pH 6, controlled by $HNO_3$), 1 M $LiNO_3$ in $H_2O$ (pH 2, controlled by $HNO_3$), and 1 mM $HNO_3$ in $H_2O$ electrolytes, respectively. (c) 7 cycles of CV in pH 6, 1 M $LiNO_3$ in $H_2O$ electrolyte. The oxidation and reduction peaks of NiHCFe electrode decrease with cycling. (d) Propylene carbonate (PC) is used as the electrolyte solvent. 1 M $LiClO_4$, 1 M $NaClO_4$, and 0.8 M $KPF_6$ are used as salts in PC.

**Table 1** The redox potentials ($E_{half}$), the potential difference between the oxidation and reduction reactions ($\Delta E$) recorded in cyclic voltammograms, and the specific capacities from galvanostatic cycling of NiHCFe electrodes in propylene carbonate and aqueous electrolytes[a]

| | PC | | | Aqueous | | |
| --- | --- | --- | --- | --- | --- | --- |
| | $E_{half}$/V | $\Delta E$/V | Specific capacity/mA h g$^{-1}$ | $E_{half}$/V | $\Delta E$/V | Specific capacity/mA h g$^{-1}$ |
| Li$^+$ | 0.327 | 0.107 | 53.4 | 0.379 | 0.049 | 57.8 |
| Na$^+$ | 0.492 | 0.111 | 49.6 | 0.583 | 0.032 | 57.4 |
| K$^+$ | 0.665 | 0.17 | 43.7 | 0.721 | 0.02 | 57.7 |

[a] The CV data were measured at 0.1 mV s$^{-1}$ and the all capacities in galvanostatic curves were characterized at 1 C.

which indicates that K$^+$ and Na$^+$ insertion are more thermodynamically favored processes.

In organic propylene carbonate-based electrolytes (PC), the same trend is observed (Fig. 2d). The insertion potential differences between the different cations in aqueous and organic electrolytes are similar due to the similarities in the solvation energies of the ions in water and PC.[30,34] There is only a single redox peak for each ion insertion process due to the lack of H$_3$O$^+$ insertion in PC and also due to the fact that ions cannot be resolved in the structure because there are no mobile solvent molecules within the structure when in PC.

The cyclic voltammetry (CV) profiles suggest very different kinetics in aqueous and organic electrolyte. The CVs in aqueous conditions show symmetric anodic/cathodic peaks that demonstrate the reversibility and fast kinetics of aqueous ion insertion. In propylene carbonate, the peaks show asymmetry and a quasi-Nernstian behavior (the difference in potential between the anodic and cathodic peaks is larger than 100 mV) due to slower kinetics of ion insertion relative to the aqueous system. This behavior can be ascribed to different ion diffusion mechanisms within the structure in aqueous and organic electrolytes.[35] A Grotthus-like mechanism may enable the extremely rapid kinetics of ion insertion in water; this has previously been suggested for driving proton conductivity in hexacyanochromates.[35] Zeolitic water molecules exist throughout the structure, and ligand water molecules bond to the N-coordinated metal ions adjacent to hexacyanometallate vacancy sites. The N-coordinated metal ion acts as a Lewis acid, and protons are carried through the 3D hydrogen-bonding network, which is composed of zeolitic water and ligand water molecules. These different properties result in very different battery performance as described in the following section.

## NiHCFe's battery performance comparison in aqueous and organic electrolyte

Galvanostatic charge–discharge curves are reported in Fig. 3. In all aqueous electrolytes, specific capacities of about 60 mA h g$^{-1}$ were obtained at 1 C. The voltage profiles reflect the properties already observed during the CV experiments. In the presence of Li$^+$ ions (Fig. 3a), the potential spans from 0.3 to 0.7 V versus SHE. In particular, the potential hysteresis associated with Li$^+$ insertion is significantly greater than that associated with Na$^+$ or K$^+$ because of the partial

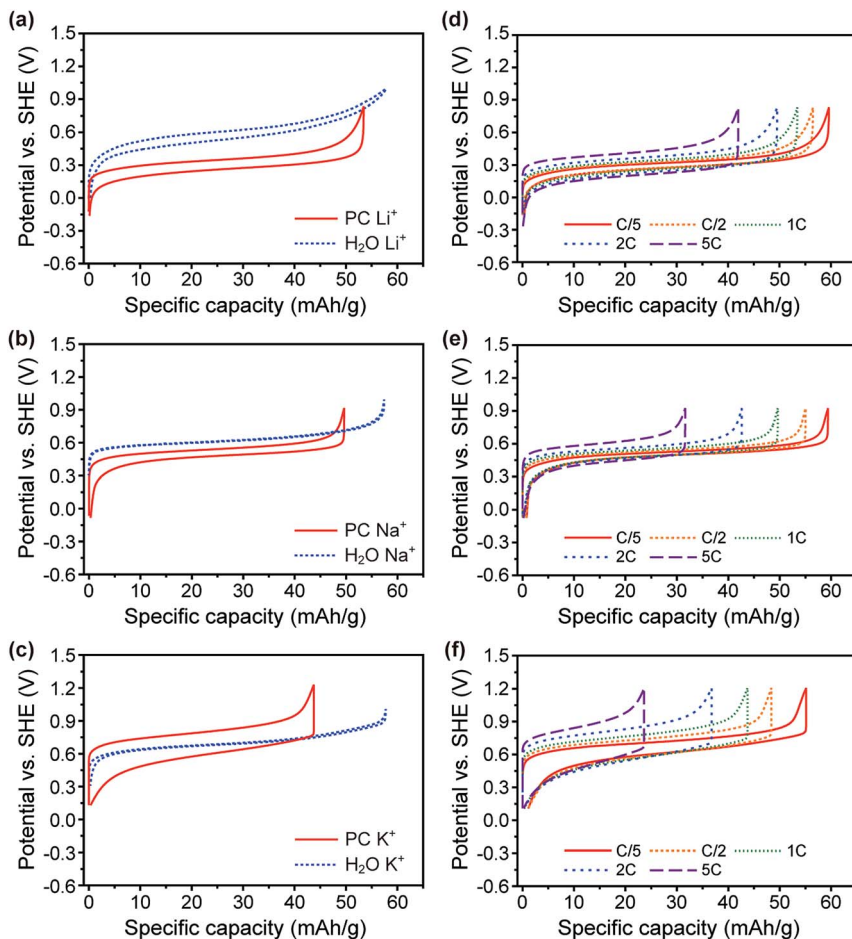Fig. 3 Comparison of hysteresis in galvanostatic potential profiles at 1 C between aqueous and PC electrolytes. (a) $Li^+$, (b) $Na^+$, and (c) $K^+$ ion systems. Typical charge and discharge potential profiles of NiHCFe electrodes at different C rates (0.2, 0.5, 1, 2, and 5 C) with (d) $Li^+$, (e) $Na^+$, and (f) $K^+$ ions in PC.

rehydration of $Li^+$ after insertion as previously described. Curves obtained in the presence of $Na^+$ (Fig. 3b) and $K^+$ (Fig. 3c) show remarkably low potential hysteresis (high energy efficiency) and a higher reaction potential in the presence of $K^+$ relative to that of $Na^+$. The rate capability of the material in the presence of $Li^+$, $Na^+$, and $K^+$/PC solutions is reported in Fig. 3d–f, respectively, and the comparison between electrolytes is summarized in Fig. 4. The results show that the kinetics are much better in aqueous than in organic electrolytes.

## Effect of the inserting ion on the kinetic features of NiHCFe's electrochemistry in aqueous electrolyte

The kinetic properties are not only affected by the nature of the solvent but also by the nature of the guest ion. To explore this effect, we have performed a set of measurements using the Swagelok experimental setup described in the
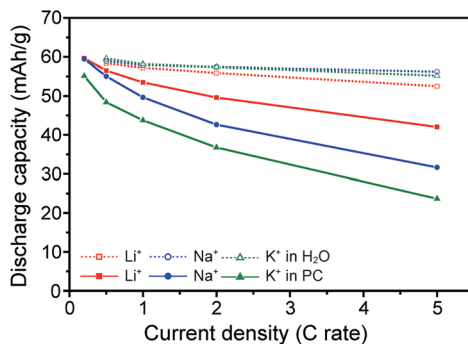
**Fig. 4** Discharge capacity retention in aqueous and PC electrolytes with different insertion ions at varying C rates.

Experimental section. The Swagelok setup, besides allowing us to perform electrochemical experiments in a convenient three-electrode setup configuration, offers a consistent distance between the positive and negative electrode, which minimizes the varying effects of electrolyte resistance on kinetics experiments. Due to the use of flat, smooth stainless steel current collectors instead of porous carbon cloth, the active material loading is lower (about 1 mg cm$^{-2}$) but still many orders of magnitude higher than that in thin film electrodes.[36] Therefore, these electrodes in the Swagelok configuration can still be considered as bulk systems.

To highlight the kinetic properties of NiHCFe in different electrolytes, we performed CV scans at different scan rates (Fig. 5). We focused our attention on aqueous electrolytes because of the better electrochemical properties and the possibility of including Rb$^{+}$ and Cs$^{+}$ in the comparison since their nitrate salts have the required solubility (1 M). Fig. 5a shows the CV profiles obtained in 1 M solutions at a 1 mV s$^{-1}$ scan rate. The peak positions are in perfect agreement with those obtained in the flooded configuration. The redox potentials corresponding to the different electrolytes are summarized in Table 2, which also reports the separation between the reduction and the oxidation peaks ($\Delta E$). In a previous study,[29] the electrochemical reactions of hexacyanometallates were thought to be diffusion-limited, but our results suggest a different kinetic limitation for NiHCFe. The peak separation is too low for a one-electron reaction under diffusion-controlled kinetic conditions.

The kinetic regime can be better understood by analyzing the relationship between the CV scan rate and the corresponding peak current. The analysis was carried out at different scan rates from 0.25 to 5 mV s$^{-1}$ for different guest ions (Fig. 5b–f). In the presence of small alkali cations (Li$^{+}$, Na$^{+}$, and K$^{+}$), very small potential shifts are observed for the redox processes, even at the highest scan rate. The corresponding peak currents show a linear relationship *versus* the scan rate (see Fig. 6a–c), which highlights the diffusionless behavior wherein the maximum current is only limited by the number of electroactive species at/in the electrode. This kind of behavior is typical of thin film electrodes,[37,38] and, to our knowledge, NiHCFe is the first case of diffusionless behavior in bulk systems. In the thin layer electrode treatment, the linear relationship between the peak current and the scan rate is ruled by:[37]
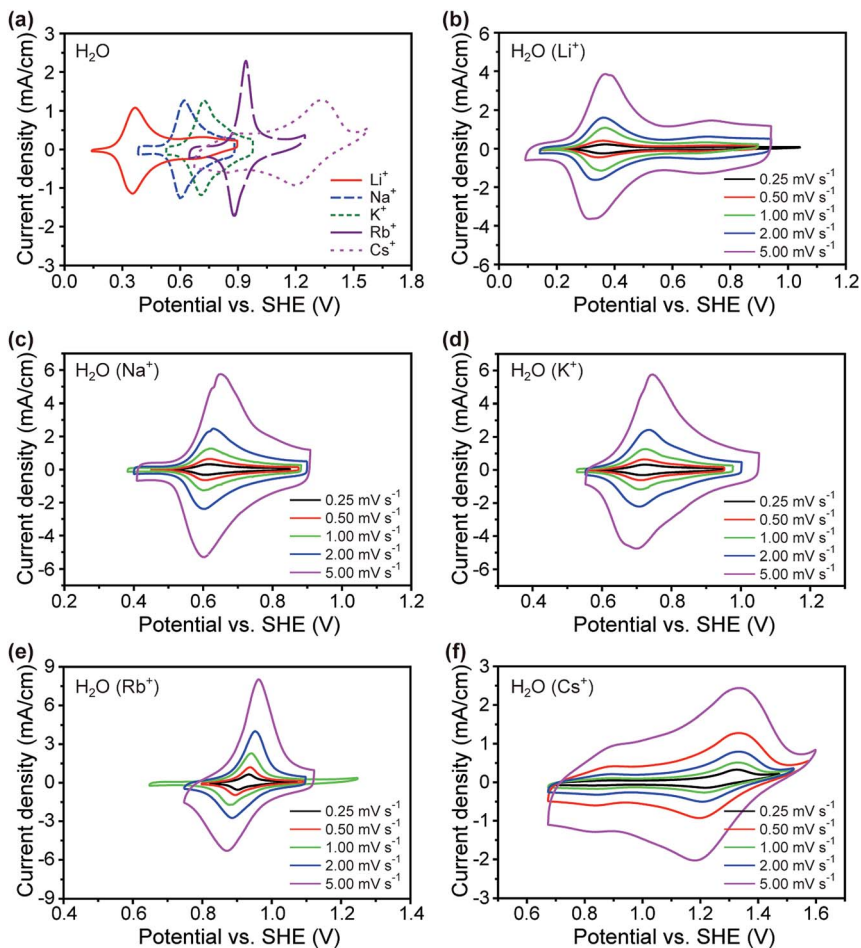
Fig. 5 CV curves of NiHCFe using the three-electrode Swagelok cell configuration in aqueous electrolytes. The scan rate is 1 mV s$^{-1}$. (a) CV curves of Li$^+$, Na$^+$, K$^+$, Rb$^+$, and Cs$^+$ ions. CV curves of (b) Li$^+$, (c) Na$^+$, (d) K$^+$, (e) Rb$^+$, and (f) Cs$^+$ ions at different scan rates from 0.25 to 5.00 mV s$^{-1}$.

Table 2 The redox potentials in different aqueous electrolytes as measured in the three-electrode Swagelok configuration

|  | $E_{half}$/V | $\Delta E$/V |
|---|---|---|
| LiNO$_3$ | 0.350 | 0.015 |
| NaNO$_3$ | 0.615 | 0.01 |
| KNO$_3$ | 0.715 | 0.01 |
| RbNO$_3$ | 0.920 | 0.06 |
| CsNO$_3$ | 1.275 (0.870[a]) | 0.12 (0.05[a]) |

[a] The CV data were measured at 0.1 mV s$^{-1}$ and stopped at 1.12 V.

$$i_{peak} = \frac{n^2 F^2}{4RT} \times A \times \Gamma_0^* \times V_{rate}$$

where $n$ is the number of electrons involved in the reaction, $F$ the Faraday constant (C mol$^{-1}$), $R$ the gas constant (J mol$^{-1}$ K$^{-1}$), $T$ the temperature (K), $A$ the surface area (cm$^2$), $\Gamma_0^*$ the concentration of active sites (mol cm$^{-2}$), and $v_{rate}$ the scan rate (mV s$^{-1}$). The $\Gamma_0^*$ parameters obtained from the slopes of the straight lines in Fig. 6a–c are used to calculate the electrode specific capacity reported in Table 2, which are in good agreement with the values obtained in Fig. 4. The reduction and reoxidation processes in the presence of both Rb$^+$ and Cs$^+$ ions show asymmetrically shaped peaks. However, the kinetic properties differ greatly between the two guest ions. In the case of Rb$^+$, the $\Delta E$ is small (around 60 mV) and comparable with the value in the diffusion-controlled kinetic regime. In fact, the peak current depends linearly on the square root of the scan rate (Fig. 6d), whose dependency is given by:[37]

$$i_{peak} = 0.4463 \times \sqrt{\frac{n^3 F^3}{RT}} \times \sqrt{D} \times C_0 \times \sqrt{V_{rate}}$$

where $D$ is the average diffusion coefficient (cm$^2$ s$^{-1}$) in the whole composition range and $C_0$ the concentration of active sites (mol cm$^{-3}$). The slope can thus be used to determine the diffusion coefficient once $C_0$ and $n$ are known. If we consider the reaction as monoelectronic and estimate $C_0$ from the specific capacity (60 mA h g$^{-1}$), we can calculate the diffusion coefficient $D$ to be $5.7 \pm 1.0 \times 10^{-6}$ cm$^2$ s$^{-1}$, which is two times lower than that of Rb$^+$ in aqueous RbCl solution ($2.06 \times 10^{-5}$ cm$^2$ s$^{-1}$)[39] but still remarkably high for solid-state diffusion.
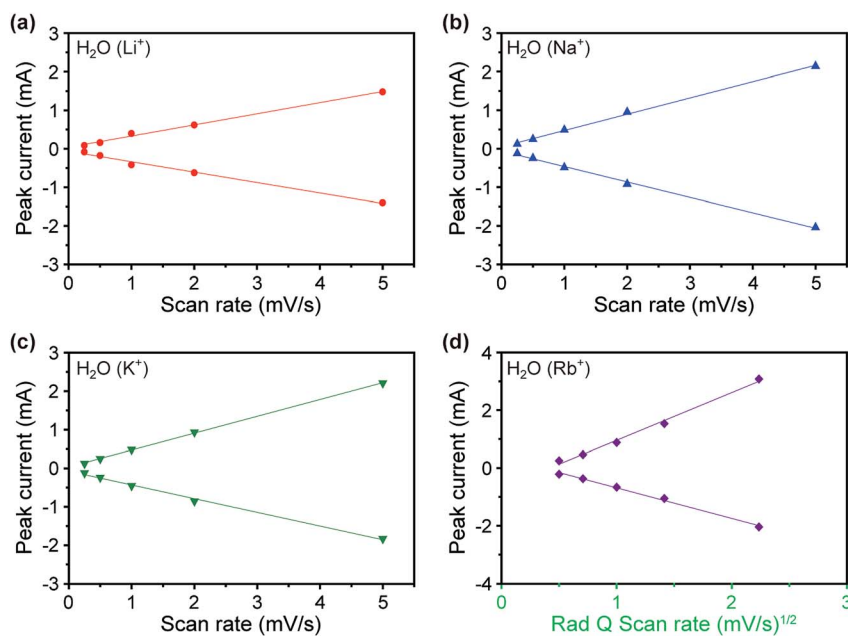


Fig. 6   The relationship between the peak currents and corresponding scan rates of (a) Li$^+$, (b) Na$^+$, (c) K$^+$, and (d) Rb$^+$ ions in aqueous electrolytes.

On the other hand, in the presence of $Cs^+$ ions the reaction is quasi-reversible, and no kinetic analysis can be carried out. The high hysteresis is a result of the size of $Cs^+$, which is larger than the channel size and smaller than the size of A-site, likely resulting in complete dehydration of the ion before insertion. The dehydration of the $Cs^+$ ion in this case is similar to the results in organic electrolytes as shown in Fig. 2d. In organic electrolytes, guest ions must also be fully desolvated before insertion, which results in high charge transfer energy.

## Conclusions

The effect of the inserting alkali ion on the electrochemical properties of NiHCFe, which has the characteristic open framework crystal structure of Prussian blue analogues, was investigated in both aqueous and organic (propylene carbonate) electrolytes. A linear relationship between the insertion potential and the size of the alkali ion has been highlighted in both electrolyte systems. In particular, a smaller insertion ion has a higher solvation energy that needs to be overcome before insertion in the host structure and therefore a lower insertion potential.

On the other hand, profound kinetic dissimilarities between the two electrolytes systems were demonstrated. CVs in aqueous conditions show symmetric anodic/cathodic peaks that demonstrate the reversibility and fast kinetics of aqueous ion insertion. Moreover, smaller alkali ions like Li, Na and K show a diffusionless behavior wherein the maximum current is only limited by the number of electroactive species at/in the electrode. This enables the minimal hysteresis in the galvanostatic charge–discharge curves (extremely high energy efficiency) and the exceptionally long cycle life exhibited by nickel hexacyanoferrate and PBAs in general.

In propylene carbonate, the CV peaks show asymmetry and a quasi-Nernstian behavior that results in poor galvanostatic cycling performance. We believe that the different behavior could be ascribed to a different diffusion mechanism in the open framework crystal structure. Therefore, an aqueous electrolyte system is needed – to guarantee the extremely long cycle life and energy efficiencies required by grid scale energy storage applications.[13]

## Acknowledgements

Johanna N. Weker, Dr Badri Shyam, and Dr Kevin H. Stone for help with synchrotron X-ray diffraction.

## Notes and references

1 J.-M. Tarascon and M. Armand, *Nature*, 2001, **414**, 359–367.
2 M. Armand and J.-M. Tarascon, *Nature*, 2008, **451**, 652–657.
3 K. Kang, Y. S. Meng, J. Bréger, C. P. Grey and G. Ceder, *Science*, 2006, **311**, 977–980.
4 H. Lee, P. Muralidharan, R. Ruffo, C. M. Mari, Y. Cui and D. K. Kim, *Nano Lett.*, 2010, **10**, 3852–3856.
5 C. Chan, H. Peng, G. Liu and K. McIlwrath, *Nat. Nanotechnol.*, 2008, **3**, 31–35.
6 P. G. Bruce, S. A. Freunberger, L. J. Hardwick and J.-M. Tarascon, *Nat. Mater.*, 2012, **11**, 19–29.
7 B. Dunn, H. Kamath and J.-M. Tarascon, *Science*, 2011, **334**, 928–935.
8 Z. Yang, J. Zhang, M. C. W. Kintner-Meyer, X. Lu, D. Choi, J. P. Lemmon and J. Liu, *Chem. Rev.*, 2011, **111**, 3577–3613.
9 G. L. Soloveichik, *Annu. Rev. Chem. Biomol. Eng.*, 2011, **2**, 503–527.
10 M. S. Whittingham, *Chem. Rev.*, 2004, **104**, 4271–4301.
11 J.-M. Tarascon, *Nat. Chem.*, 2010, **2**, 510.
12 S.-W. Kim, D.-H. Seo, X. Ma, G. Ceder and K. Kang, *Adv. Energy Mater.*, 2012, **2**, 710–721.
13 C. Barnhart and S. Benson, *Energy Environ. Sci.*, 2013, **6**, 1083–1092.
14 W. Li, J. Dahn and D. Wainwright, *Science*, 1994, **264**, 1115–1118.
15 R. Ruffo, C. Wessells, R. A. Huggins and Y. Cui, *Electrochem. Commun.*, 2009, **11**, 247–249.
16 J. Luo, W. Cui, P. He and Y. Xia, *Nat. Chem.*, 2010, **2**, 760–765.
17 Y. Lu, L. Wang, J. Cheng and J. B. Goodenough, *Chem. Commun.*, 2012, **48**, 6544–6546.
18 L. Wang, Y. Lu, J. Liu, M. Xu, J. Cheng, D. Zhang and J. B. Goodenough, *Angew. Chem., Int. Ed.*, 2013, **52**, 1964–1967.
19 T. Matsuda, M. Takachi and Y. Moritomo, *Chem. Commun.*, 2013, **49**, 2750–2752.
20 C. D. Wessells, R. A. Huggins and Y. Cui, *Nat. Commun.*, 2011, **2**, 550.
21 R. Y. Wang, C. D. Wessells, R. A. Huggins and Y. Cui, *Nano Lett.*, 2013, **13**, 5748–5752.
22 C. D. Wessells, S. V. Peddada, M. T. McDowell, R. a. Huggins and Y. Cui, *J. Electrochem. Soc.*, 2012, **159**, A98–A103.
23 C. D. Wessells, S. V Peddada, R. A. Huggins and Y. Cui, *Nano Lett.*, 2011, **11**, 5421–5425.
24 H. M. Rietveld, *J. Appl. Crystallogr.*, 1969, **2**, 65–71.
25 A. C. Larson and R. B. Von Dreele, *Los Alamos Natl. Lab. Rep.*, **LAUR 86–74**, 1994.
26 B. H. Toby, *J. Appl. Crystallogr.*, 2001, **34**, 210–213.
27 G. Gritzner, *Pure Appl. Chem.*, 1990, **62**, 1839–1858.
28 Y. Yang, C. Brownell and N. Sadrieh, *Clin. Toxicol.*, 2007, **45**, 776–781.
29 F. Scholz and A. Dostal, *Angew. Chem., Int. Ed. Engl.*, 1996, **34**, 2685–2687.
30 A. Domenech, N. Montoya and F. Scholz, *J. Electroanal. Chem.*, 2011, **657**, 117–122.

31 M. Tissandier and K. Cowen, *J. Phys. Chem. A*, 1998, **5639**, 7787–7794.

32 J. Mähler and I. Persson, *Inorg. Chem.*, 2012, **51**, 425–438.

33 Y. Marcus, *J. Chem. Soc., Faraday Trans.*, 1991, **87**, 2995–2999.

34 M. Salomon, *J. Phys. Chem.*, 1970, **74**, 2519–2524.

35 S.-I. Ohkoshi, K. Nakagawa, K. Tomono, K. Imoto, Y. Tsunobuchi and H. Tokoro, *J. Am. Chem. Soc.*, 2010, **132**, 6620–6621.

36 A. Eftekhari, *J. Power Sources*, 2004, **132**, 291–295.

37 A. J. Bard and L. R. Faulkner, *Electrochemical methods: fundamentals and applications*, John Wiley, New York, 2nd edn, 1980.

38 J. Heinze, B. Frontana-Uribe and S. Ludwigs, *Chem. Rev.*, 2010, **110**, 4724–4771.

39 H. Harned and M. Blander, *J. Am. Chem. Soc.*, 1953, **159**, 1951–1953.